

Reconfigurable Rainbow PIV for 3D Flow Measurement

Jinhui Xiong Qiang Fu Ramzi Idoughi Wolfgang Heidrich
King Abdullah University of Science and Technology
jinhui.xiong@kaust.edu.sa

Abstract

In recent years, 3D Particle Imaging Velocimetry (PIV) has become more and more attractive due to its ability to fully characterize various fluid flows. However, 3D fluid capture and velocity field reconstruction remain a challenging problem. A recent rainbow PIV system encodes depth into color and successfully recovers 3D particle trajectories, but it also suffers from a limited and fixed volume size, as well as a relatively low light efficiency. In this paper, we propose a reconfigurable rainbow PIV system that extends the volume size to a considerable range. We introduce a parallel double-grating system to improve the light efficiency for scalable rainbow generation. A varifocal encoded diffractive lens is designed to accommodate the size of the rainbow illumination, ranging from 15mm to 50mm. We also propose a truncated consensus ADMM algorithm to efficiently reconstruct particle locations. Our algorithm is 5× faster compared to the state-of-the-art. The reconstruction quality is also improved significantly for a series of density levels. Our method is demonstrated by both simulation and experimental results.

1. Introduction

A fully characterized fluid flow is essential for studying fluid properties in the field of fluid dynamics, and for flow editing and re-simulations in other applications. However, investigating complex and three-dimensional fluid phenomena in an easy way remains unsolved. Tomographic Particle Imaging Velocimetry (Tomo-PIV) [4, 11] has been extensively studied in recent decades, and its wide applicability to imaging various fluid phenomena has been demonstrated. Specifically, Tomo-PIV makes use of multiple cameras (normally 4 – 6 cameras) that observe the volume from different perspectives, and reconstructs three dimensional intensity fields and three components of the velocity fields over a 3D measurement volume (3D-3C) by means of multiplicative reconstruction technique (MART) and correlation-based algorithms respectively. Although Tomo-PIV has several advantages, such as high spatial resolution, and is

regarded as a standard technique in fluid dynamics, it still suffers from severe limitations that limit its usage. First among these is the complexity for setting up and calibrating the whole system, which usually takes a considerable amount of efforts. Another practical issue is depth-of-field, which restricts it from working on volumes with relatively large depth that typically ranges from 10mm to 20mm [5]. Moreover, it would be impractical to set up multi-camera systems for many types of flows constrained by limited optical access, in which situation a single-camera system is preferred.

Recently, single-camera approaches were proposed on a basis of the plenoptic camera (or light field camera) [9, 7], addressing part of the issues arisen from Tomo-PIV. Specifically, a plenoptic camera records the full 4D light fields, which are generated from the scattered light of seeded particles in the flow. Herein, one can digitally reconstruct the particle locations using ray-tracing based algorithms [8, 5, 3, 12]. Overall, by using a light field camera, it allows a dramatically simplified setup overcoming the optical access limitation. Furthermore, it can digitally refocus the images and thus allows a relatively large depth-of-field even for a large aperture lens. While as a compromise, the LF-PIV approach sacrifices spatial resolution for angular information, in order to achieve sufficient axial resolution. Furthermore, storing and processing 4D light field data is computationally expensive and exhibits heavy memory usage. Besides, light field camera commonly has low frame rates. All of the above mentioned drawbacks make time-resolved reconstruction of non-stationary fluid flows an intractable issue.

A further simplified setup using a single off-the-shelf RGB camera has been presented in [13]. This Rainbow-PIV system simultaneously achieves high lateral resolution and all depths in focus without significant light loss, and also it is able to reconstruct time-resolved flows based on captured video frames. In short, it illuminates the volume using a rainbow light, which is produced by passing a white beam through a linear variable filter, such that the depth information is encoded by color. On the acquisition side, a custom designed diffractive optical element (DOE) man-

ages a wavelength-selective focus so that all light planes are in focus at the same time. Afterwards, a joint optimization solver for particle distribution and velocity vector fields reconstruction is utilized for time-varying 3D-3C fluid velocity measurements. It also demonstrates its applications in different flow scenarios and reveals a compelling and robust reconstruction accuracy.

Nevertheless, the use of the linear variable filter for rainbow generation limits the depth range of the optical setup to a very specific size. Changing the depth range would require replacing the linear filter with a different version and changing the collimating optics, which involves rather large changes to the optical system. Also in this setup, the rainbow illumination is generated through absorption of unwanted wavelengths in the linear filter, which is a very energy inefficient process. These limitations restrict the above mentioned system from being adopted to an observing volume with various depth ranges. A flexible fluid measurement system would be favored for its applicability to flow phenomena occurred in various length scales. Considering this, we seek to use two off-the-shelf blazed gratings, and further design an encoded diffractive optics (see [6]) to construct an easily reconfigurable PIV system. Specifically, we make the following contributions:

- We propose a single-camera 3D-3C PIV system with a scalable, reconfigurable rainbow illumination.
- We design and fabricate adjustable diffractive optics to focus all light planes for a reconfigurable rainbow volume.
- We propose a computationally efficient and memory friendly solver for high-precision 3D particle reconstruction.
- We demonstrate the scalability of our hardware setup on real fluid scenarios.

2. Overview

In the following, we provide an overview of our designed system that meets the rainbow scalability requirement, and improves the particle position reconstruction performances.

To achieve reconfigurability of the rainbow volume, we require changes to both the illumination and the imaging system. In other words, the fluid volume containing seeded particles should be illuminated by a parallel rainbow beam with readily modifiable size. Furthermore, the imaging system should have an easily adjustable focal length, to ensure that for each rainbow size all particles are in-focus. Figure 1 illustrates our optical setup. The solution selected to generate a reconfigurable rainbow is based on the use of two parallel blazed gratings, combined to a white light source, a collimator and a cylindrical lens. Indeed, the size

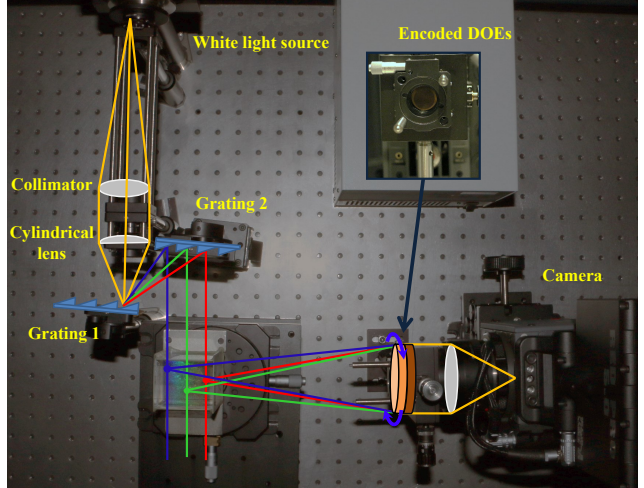


Figure 1: Reconfigurable Rainbow PIV setup. The illumination system, based on two parallel blazed gratings, allows the control of the rainbow’s width. Meanwhile, a varifocal lens is designed to have a wavelength-selective focus adjustable according to the size of the illuminated volume.

of the rainbow is controlled by the distance between the two gratings as explained in Section 4.1. On the other hand, an encoded lens composed of two diffractive optical elements and a refractive lens is used to ensure that all colored planes of the rainbow will be in-focus. The equivalent focal length of this encoded lens is governed by the relative angle between the two DOEs.

The captured images are then used to reconstruct 3D particle locations in spatial domain. Specifically, it solves an inverse problem of the image formation model which formulates the imaging process from particle locations to the observed image. After obtaining two consecutive particle distributions, volumetric flow reconstruction is performed, using a modified Horn-Schunck optical flow model. A modified solver (truncated consensus ADMM) for particle distribution retrieval is proposed in the consideration of computational efficiency and the reconstruction quality.

3. Reconstruction

3.1. Particle Position Reconstruction

Following the image formation model from [13], particles in the volume are illuminated by wavelength-dependent (denoted as λ) light sheets, which are physically dependent on the depth of particle locations, such that the third dimension (z coordinate) of a specific illuminated particle can be determined from its spectral information. The occupancy probability of a specific voxel is described by $P(\xi, \lambda)$, where λ indicates on which light plane the voxel locates and $\xi = (x, y)$ indicates the 2D spatial position in

that light plane. Moreover, a RGB camera is employed for capturing the regions of interest, thus the response of the camera to the illuminated particles can be modeled as a series of point spread functions (PSFs), denoted as $K_c(\lambda)$, which vary from the color channels c ($c \in \{r, g, b\}$) and wavelengths. The convolution operator for the PSFs can be further formulated into matrix $\mathbf{A} = [\mathbf{A}_r; \mathbf{A}_g; \mathbf{A}_b]$. The objective is to reconstruct the particle probability distributions. Specifically, we solve the following minimization problem:

$$(\mathbf{p}^*) = \underset{\mathbf{p}}{\operatorname{argmin}} \quad \frac{1}{2} \|\mathbf{Ap} - \mathbf{i}\|_2^2 + \alpha \|\mathbf{p}\|_1, \quad (1)$$

where $\mathbf{i} = [\mathbf{i}_r; \mathbf{i}_g; \mathbf{i}_b]$ is the stacked vector for the observed RGB image, \mathbf{p} is the vectorization of 3D particle distributions, and α regulates the sparsity of the reconstructed particles in spatial domain.

The above minimization problem refers to the basic LASSO algorithm, which can be solved by the ADMM framework [1], as in [13]. However this basic solution incurs a significant cost both on terms of computational effort and memory consumption when dealing with a large concatenated matrix \mathbf{A} . Although some matrix-free solvers, for instance conjugate gradient, can be applied to avoid explicitly storing the coefficient matrix, the computational cost is still significant. To ease both memory consumption and computational cost, we introduce a consensus based ADMM solver that allows us to split the problem into smaller chunks based on the spectral response of the camera sensor. These individual parts can be solved almost independently.

Consensus ADMM solver. Consensus ADMM has been recently used to solve distributed optimization problems [14, 1], and large-scale/high-dimensional feature learning based image processing tasks [2]. In particular, it solves an optimization problem involving a composite objective $\sum_j f_j(\mathbf{x}_j)$, where $f_j : \mathbb{R}^n \rightarrow \mathbb{R}$ refers to j^{th} component of the entire objective, and \mathbf{x}_j are the corresponding local variables. The local variables are all constrained by a common global variable \mathbf{y} , written as $\mathbf{x}_j = \mathbf{y}$. For a simple variation of the objective function with an additional regularization term g , the problem can be expressed as:

$$\begin{aligned} & \text{minimize} \quad \sum_j f_j(\mathbf{x}_j) + g(\mathbf{y}) \\ & \text{subject to} \quad \mathbf{x}_j = \mathbf{y}, \end{aligned} \quad (2)$$

We can fit our particle reconstruction model into the above consensus problem by decomposing it based on color channel, such that each subproblem corresponds to a single color channel. Specifically, for the problem in Eq. (1), $f_c(\mathbf{p}_c) = \frac{1}{2} \|\mathbf{A}_c \mathbf{p}_c - \mathbf{i}_c\|_2^2$ and $g(\mathbf{y}) = \alpha \|\mathbf{y}\|_1$. The consensus ADMM solver is expressed in Algorithm 1.

Algorithm 1 Consensus ADMM for solving Eq. 2

```

1: for  $k = 1$  to  $N$  do
2:   // p-update step (ridge regression)
3:    $\mathbf{p}_c^{k+1} \leftarrow (\mathbf{A}_c^T \mathbf{A}_c + \rho \mathbb{I})^{-1} (\mathbf{A}_c^T \mathbf{i}_c + \rho (\mathbf{y}^k - \mathbf{q}_c^k))$ 
4:   // y-update step (soft thresholding)
5:    $\mathbf{y}^{k+1} \leftarrow (\bar{\mathbf{p}}^{k+1} + \bar{\mathbf{q}}^k - \frac{\alpha}{3\rho})_+ - (-\bar{\mathbf{p}}^{k+1} - \bar{\mathbf{q}}^k - \frac{\alpha}{3\rho})_+$ 
6:   // scaled dual variables update
7:    $\mathbf{q}_c^{k+1} \leftarrow \mathbf{q}_c^k + \mathbf{p}_c^{k+1} - \mathbf{y}^{k+1}$ 
8: end for

```

Here, $\bar{\mathbf{p}}$ and $\bar{\mathbf{q}}$ denote the averaged value of \mathbf{p}_c and \mathbf{q}_c over color channels respectively. Each subproblem tackles the reconstruction step in one color channel, and hence it becomes less computationally intensive and more memory friendly. While an issue referred to “over averaging” arises when averaging the local variables in y-update step of Algorithm 1. This issue comes from the fact that the generated rainbow covers a broadband visible spectrum, ranging from red to blue light. Herein, one color channel only covers part of the observing volume in axial direction, for instance red covers the front part of the volume, blue covers the rear part and green covers the middle part. Thus each subproblem can only reconstruct particles over the regions which are referred by the associated color channel. Therefore, averaging the solutions to the subproblems leads to degraded results, which causes the “over averaging” issue. To overcome this issue, we present a truncated consensus ADMM solver, besides, it achieves higher computational efficiency.

Truncated Consensus ADMM solver. The general idea for the proposed truncated consensus solver is illustrated in Figure 2. Since one color channel provides partial information of the particle distributions in the volume along z -axis, we can discard those useless regions and retain the regions with the corresponding color information for each channel. Therefore, every modified subproblem only reconstructs partial particle distributions. Recall the notations in Figure 2, \mathbf{A}_c^{tr} denotes the truncated matrix of \mathbf{A}_c and \mathbf{p}_c^{tr} denotes the particle distributions referred by the color channel c .

Moreover, depth-dependent weights will be applied for the L_1 penalty term in order to compensate for the camera spectral sensitivity. For instance, the spectral response of the green channel of the camera sensor may be effective to wavelengths roughly ranging from 500nm to 600nm, while it has the peak response at 530nm. This will lead to a non-uniform distributions of reconstructed particles, which are preferred to be placed at wavelength levels exhibiting large response. The compensatory weighting term enables us to ease the biased reconstruction results, which is expressed as:

$$w_c(\lambda_i) = \frac{\|K_c(\lambda_i)\|_2^2}{\max_{i \in 1, \dots, M} (\|K_c(\lambda_i)\|_2^2)} \alpha, \quad (3)$$

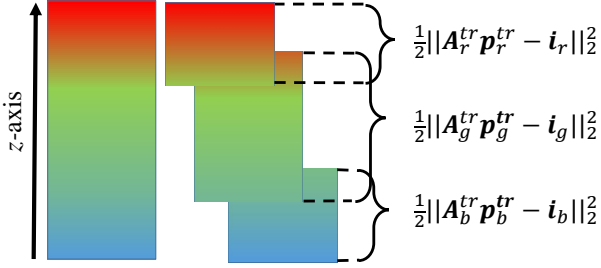


Figure 2: Illustration of the truncated consensus solver. Each subproblem only tackles part of the observing volume which is referred by the involved color channel.

where $w_c(\lambda_i)$ refers to the weights of the c color channel at depth level of wavelength λ_i , and M is the number of discretized levels in axial direction. As we can observe, this formula assigns smaller penalties to the wavelength levels with less sensitive spectral response and larger penalties to levels with higher sensitivity.

3.2. Volumetric Flow Reconstruction

The algorithm used for tracking the fluid motion is adopted from [13], except that we only work on two frames, instead of a video sequence, to validate the scalability of our proposed PIV system. The tracking algorithm is a variant of standard Horn-Schunck model, in which the brightness constancy term is replaced by a particle presence consistency term, and also the divergence-free constraint is taken into account.

Specifically, we solve the following optimization problem

$$\mathbf{u}^* = \underset{\mathbf{u}}{\operatorname{argmin}} \int_{\Omega} \frac{\mathbf{p}_1}{2} \odot (\mathbf{p}_1 - \mathbf{p}_2(\mathbf{u}, -\Delta t))^{\circ 2} d\Omega + \beta \|\nabla \mathbf{u}\|_2^2 + \Pi_{C_{\text{DIV}}}(\mathbf{u}), \quad (4)$$

where \odot and \circ^2 are component-wise (Hadamard) operators. The terms in this optimization problem are respectively a Horn-Schunck style ‘‘photoconsistency’’ term on the particle occupancy probabilities, an advection term, and an incompressibility term. We refer to [13] for detailed derivations of these terms. The method for solving this optimization problem is reproduced in Algorithm 2 for the sake of completeness. For lightening the notation, we define

$$\begin{aligned} \hat{\mathbf{p}}_2^k &= \mathbf{p}_2(\mathbf{u}^k, -\Delta t) \\ \mathbf{H} &= \mathbf{p}_1 \odot (\nabla \hat{\mathbf{p}}_2^k)^{\circ 2} + 2\beta \nabla^2 \\ \mathbf{t} &= \mathbf{p}_1 \odot (\hat{\mathbf{p}}_2^k - \mathbf{p}_1 - \nabla \hat{\mathbf{p}}_2^k \mathbf{u}^k) \nabla \hat{\mathbf{p}}_2^k \end{aligned}$$

Algorithm 2 ADMM for solving Eq. 4

```

1: for  $k = 1$  to  $K$  do
2:   // u-minimization step
3:    $\mathbf{u}^{k+1} \leftarrow (\rho \mathbf{H} + \mathbb{I})^{-1}(\mathbf{y}^k - \mathbf{q}^k - \rho \mathbf{t})$ 
4:   // pressure projection step
5:    $\mathbf{y}^{k+1} \leftarrow \Pi_{C_{\text{DIV}}}(\mathbf{u}^{k+1} + \mathbf{q}^k)$ 
6:   // scaled dual variables update
7:    $\mathbf{q}^{k+1} \leftarrow \mathbf{q}^k + \mathbf{u}^{k+1} - \mathbf{y}^{k+1}$ 
8: end for

```

4. Hardware setup

4.1. Double Blazed Gratings Rainbow Generation

In this subsection, we explain our approach to generate a rainbow beam to illuminate the tank. This rainbow volume should consist of a stack of parallel, nearly monochromatic planes, where the density of the planes (and therefore the thickness of the rainbow volume) is easily adjustable in size. Furthermore, the system should provide a good light efficiency. To meet these requirements we propose to use a setup based on two parallel gratings respecting the blaze condition, as shown in Figure 3.

A white light beam is generated by a plasma light source combined with a liquid light guide (HPLS245, Thorlabs). The beam becomes parallel after passing through the collimator. Then a cylindrical lens is employed to focus the light into a line that will reach the first blazed grating. After being diffracted by the first grating, the obtained rainbow beam is divergent and spreads out in the perpendicular direction to the rainbow plane. A second blazed grating, identical and parallel to the first one, will diffract the rainbow beam with the same angles as the previous one, yielding a parallel rainbow beam.

The blazed gratings are adopted in our setup because they concentrate the maximum optical power for a given diffraction order (the first order in our case), while the energy of other orders (including the zeroth order) is minimized. The selected blazed gratings have the following characteristics: blaze wavelength 500nm, blaze angle 17°27', 1200 grooves/mm, dimension 50mm × 50mm × 9.5mm and 60 – 80% grating efficiency at the blaze wavelength. The width of the obtained rainbow beam can be simply controlled by the distance between the two gratings.

4.2. Encoded Diffractive Optical Elements

Once the particles of interest are illuminated by the reconfigurable rainbow light generated by the double blazed gratings, a varifocal DOE lens is necessary to adapt to the changing volume length. This varifocal DOE lens should be able to continuously adjust to the color depth of field all over along the volume range. Thereby, a single DOE as used in [13] is not sufficient. We propose to adopt the

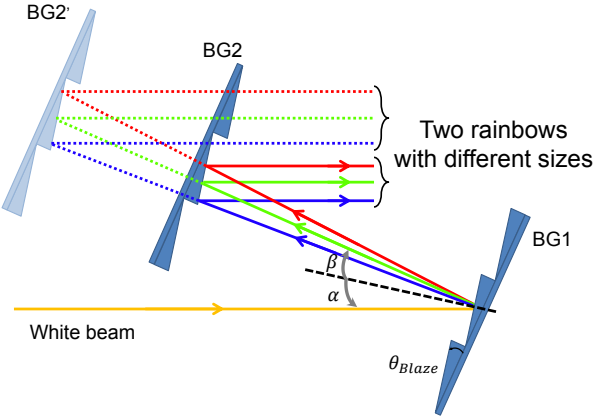


Figure 3: Illustration of rainbow generation using two parallel blazed gratings (BG1 and BG2 / BG2'). A parallel white beam reaching BG1 with an incidence angle (α) equal to the blaze angle (θ_{Blaze}), is diffracted at the same angle (β) for the blazed wavelength (green ray). The second diffraction occurs at BG2 / BG2' with the same angles for each wavelength. The obtained rainbow is then parallel, and its width is controlled by the distance between the two gratings.

encoded diffractive lens as previously reported by Heide et al. [6] to realize the varifocal DOE lens.

An encoded diffractive optical element (EnDOE) consists of two DOEs that are optimized to form the phase function of an ideal lens when the two are aligned face-to-face. The focal lengths of the EnDOE are encoded in the relative rotation angles between the two components. Over a specific angle range $0 \leq \theta_{\min} \leq \theta_{\max} \leq \pi$, the focal length can be designed in the range of $[-f_{\max}, -f_{\min}] \cup [f_{\min}, f_{\max}]$.

For a given volume range $[L_{\min}, L_{\max}]$, we need to design the focal length range of the EnDOE. Consider the optical layout in Figure 4 (a). Assume the wavelength range of the rainbow illumination is $[\lambda_1, \lambda_2]$. The EnDOE is designed at wavelength λ_0 , which lies in the middle of the range. The nominal focal length of the EnDOE is $f_{E,0}$, and the focal length of the refractive lens is f_L for all the wavelengths (here we assume the refractive lens is achromatic). For wavelength λ other than the design wavelength, the corresponding focal length of the EnDOE is determined by $\lambda f_{E,\lambda} = \lambda_0 f_{E,0}$. Applying the Gaussian lens formula, we have

$$\frac{1}{s(\lambda)} + \frac{1}{s'} = \frac{\lambda}{\lambda_0 f_{E,0}} + \frac{1}{f_L} - d \frac{\lambda}{\lambda_0 f_{E,0}} \frac{1}{f_L}, \quad (5)$$

where s and s' are respectively the object distance and image distance measured from the principal plane. The right hand side of Eq. (5) is the effective focal length of the entire system, and d is the distance between the EnDOE and the

refractive lens. Taking derivatives over both sides of Eq. (5) and doing simple re-arrangement, we have

$$L = \Delta s \approx \left| \frac{f_L - d}{\lambda_0 f_L f_{E,0}} \right| s_0^2 \Delta \lambda, \quad (6)$$

where s_0 is the object distance at design wavelength λ_0 .

We design the rainbow illumination in the range between 460nm and 660nm. The refractive lens is a 50mm Canon DSLR lens. We place the particles at $s_0 = 220\text{mm}$ in front of the lens to keep a compact system. Ideally, the EnDOE and the refractive lens should be as close to each other as possible. In practice, there is a certain distance caused by the mechanical mounts. We approximate this distance $d \approx 5\text{mm}$. The actual volume size depends on all the factors indicated by Eq. (6).

As shown in Figure 4 (b), the volume length ranges roughly from 15mm to 75mm as $f_{E,0}$ changes from $\pm 1000\text{mm}$ to $\pm 200\text{mm}$. Considering the fabrication constraints, we design the focal length range as $(-\infty, -300] \cup [300, \infty)\text{mm}$. We still keep a considerable volume range from 15mm to 50mm.

The phase functions of the two constituent DOEs are optimized by complex matrix factorization [6]. In the design focal length range, we sample at 6 focal lengths, and calculate the respective rotation angles. The target phase functions are ideal lens phase functions at the corresponding focal lengths. Due to the symmetry of rotation angles, we choose the angle range to be as large as possible, such that the focal length variation with angles are not too sensitive to small deviations. The optimized rotation angle range is $[-114^\circ, 114^\circ]$.

Since fabricating continuous height profiles on glass substrates are challenging, we exploit multi-level photolithography techniques to fabricate the EnDOE. We first convert the optimized phase profiles to 16-level discrete phase functions. The drop in diffraction efficiency caused by this discretization could be significant if fewer levels are used, while 16-level profiles are already able to approximate the continuous profile very well [6, 10]. Each fabrication cell in the DOE is $2\mu\text{m}$, and the apertures of both DOEs are 16mm . All the samples are fabricated on 0.5mm thick fused silica wafers with a 200nm thick, Chromium aperture (16mm diameter) to prevent stray light.

5. Results

5.1. Calibration

Since wavelength changes approximately linearly in distance along longitudinal direction, we can uniformly discretize the volume in wavelength domain, and one discrete wavelength level is associated with a depth layer. It is essential to obtain the camera response to each of the wavelength level, and thus one can retrieve the depth information from

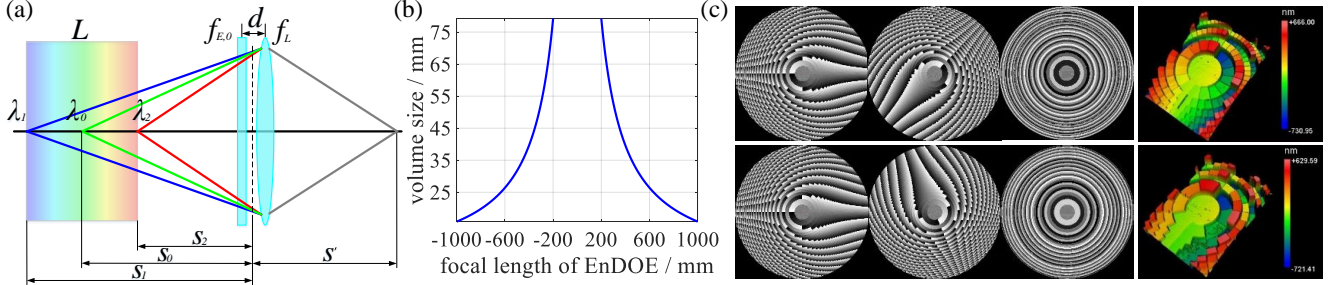


Figure 4: Optical system. (a) The combination of the EnDOE and refractive lens bring all the wavelengths to a common focal plane. (b) The volume size is approximately inversely proportional to the nominal focal length of EnDOE. (c) The two constituent DOEs (left) at rotation angles 114° (top) and -23° (bottom) create lens profiles of 300mm and -1500mm respectively. 3D profiles (right) of the fabricated DOEs was taken by Zygo NewView 7300.

captured data. In our setup, rainbow with spectrum ranging from 460nm to 660nm was generated. We discretize the spectral range into 20 levels, resulting in a spectral resolution of $10\text{nm}/\text{layer}$. When calibrating the camera response at one particular wavelength level, one can either physically block the rest wavelengths or use a wavelength filter, but the former one is preferred in our experiments as it has no extra energy loss. Similar to the work in [13], a RGB camera is applied for calibration and frame data capture, such that each PSF refers to a color image. In our setup, however, the calibration should be re-performed after changing the rainbow size.

5.2. Simulation Results

In order to quantitatively evaluate the reconstruction accuracy of the particle retrieval algorithm, we synthetically generate a number of three-dimensional particles, employ the calibrated PSFs and add Gaussian white noise of variance 0.001 to produce a simulated observed image. The reconstruction accuracy is examined by the metric of quality factor (Q), which refers to the normalized correlation coefficient of the real and reconstructed probability fields, given by

$$Q = \frac{\sum \mathbf{p} \cdot \mathbf{p}^*}{\sqrt{\sum (\mathbf{p})^2 \cdot \sum (\mathbf{p}^*)^2}} \quad (7)$$

where \mathbf{p} and \mathbf{p}^* denote the reconstructed and ground truth probability fields respectively. The simulation is proceeded on a volume of dimensions $100 \times 100 \times 20$ with different seeding densities. In the truncated approach, color information with $\|K_c(\lambda_i)\|_2^2 \leq 0.25$ is discarded. We compare the proposed truncated ADMM solver (“Trun-ADMM”), with the standard ADMM solver “ADMM” and consensus ADMM solver “CADMM” under the same parameter settings ($\alpha = 0.05$, $\rho = 1$). The results are shown in Figure 5(a), where the solid horizontal line ($Q = 0.75$) defines the base line for a sufficiently accurate reconstruction result [4]. It suggests that the proposed method reveals a

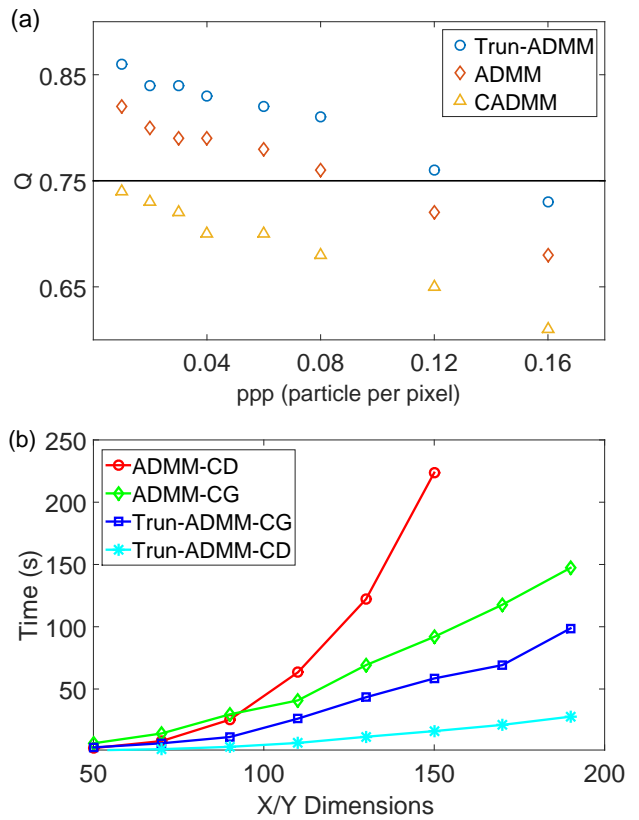


Figure 5: (a) Reconstruction quality factor (Q) versus a number of seeding densities (ppp) for different approaches. The solid horizontal line means the criterion for a reasonably accurate reconstruction. (b) Execution time for ADMM solver and Trun-ADMM solver using conjugate gradient (CG) and Cholesky decomposition (CD) respectively.

considerable improvement in reconstruction quality at all densities, while that of consensus solver is degraded significantly due to the “over averaging” issue.

We then evaluate the execution time of ADMM solver and Trun-ADMM solver for various X/Y dimensions. Conjugate gradient (CG) and Choleskey decomposition (CD) are independently applied for those two solvers to deal with the linear system of line 3 in Algorithm 1. Note that CG is implemented as a matrix-free solver and CD is preconditioning factorized, which is not counted in the running time. It takes around 31 and 36 iterations to reach the same stopping criteria for “ADMM” and “Trun-ADMM”, respectively. The results of the execution time are shown in Figure 5(b). The processing time for “ADMM-CD” increases dramatically with the dimensions, and for CG methods it increases moderately, roughly in linear. Even though the proposed truncated consensus solver (“Trun-ADMM-CD”) takes more iterations, it still achieves higher computational efficiency, especially realizing about 5× speedup over “ADMM-CG”, which is a standard way for solving this type of problem.

5.3. Refocusing

We evaluate the reconfigurability of our system by two experiments with various rainbow sizes, 50mm and 30mm, the results for which are shown in Figure 6. We can observe that with the usage of EnDOE, the images are well focused in both cases even with a large aperture, while the lens-only setup fails to focus on all particles with the same f-number. Although we can reduce the aperture size for a larger depth-of-field, as a tradeoff, the light efficiency is sacrificed and get poorer images. It should be noted that due to the diffraction efficiency, some light energy lost in the camera side, however, we can still obtain sufficiently high quality images comparable to reducing the aperture. We clarify that the size of our proposed system is not limited on the two test examples, but can be adjusted continuously from 15mm to 50mm.

5.4. Fluid Flow Measurements

At last we test our system and algorithms on real fluid flows to verify the ability for measuring flows within a volume with alterable depth ranges. The experiments take place on a test section in the size of $40\text{mm} \times 20\text{mm}$ ($x \times y$), and the size of z dimension varies with the generated rainbow. We proceed on the datasets as partially shown in Section 5.3, such that the size in axial direction is 30mm or 50mm. The working volume is discretized into grids with resolution of $400 \times 200 \times 20$, therefore, the voxel pitch in $x - y$ plane is $100\mu\text{m}$, and the pitch size in z -axis is 1.5mm or 2.5mm respectively for two generated rainbows. The pictures are captured at a frame rate of 30 fps, and the seeding density is about 0.03 ppp. The parameters for reconstructing the probability fields are the same as listed in Section 5.2. As for reconstructing volumetric flow, the parameters are common for all experiments: $\beta = 5e^{-6}$, $\rho = 1$, and

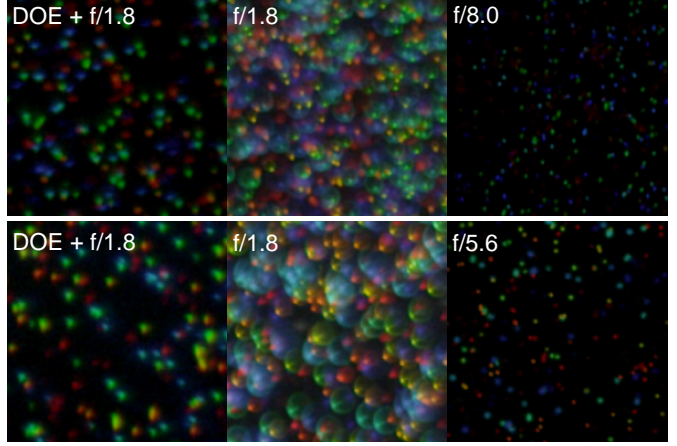


Figure 6: Images captured using the encoded DOE with lens (DOE+f/#) and lens-only (f/#) with different aperture settings. The first and second rows show the captured image with rainbow size of 50mm and 30mm respectively. Left: Encoded DOE and lens with f/1.8 since the depth-of-field of EnDOE setup is not affected by the aperture size (see Eq. 5), the largest available aperture was chosen to maximize the light efficiency. Middle: lens-only with an aperture of f/1.8. While the light efficiency matches that of our setup, depth-of-field blur is significantly worse. Right: lens-only with stopped down apertures of f/8.0 (top) and f/5.6 (bottom). Here the blur is approximately matched to our setup, but the light efficiency is decreased by a factor of 19.7 and 9.6, respectively.

the ADMM iteration is 3. The running time for the first step is about 60 seconds for each frame, and for flow reconstruction is roughly 40 minutes on a 2.50Ghz Intel Xeon E5-2680 CPU with 128GB RAM. The reconstructed flow vectors for different flow phenomena in an alterable volume size are visualized in Figure 7, and they coincide well with the real fluid flows. These results successfully demonstrate the feasibility of our proposed system in fully characterizing the 3D flow velocities for fluid scenarios in arbitrary volume size within designed depth range.

6. Conclusion

In this paper we have demonstrated a reconfigurable rainbow PIV system that can efficiently track particle flows in 3D with a considerable range of volume sizes. Compared to existing PIV methods, our system is easy to implement, and is much more flexible and re-configurable. We introduce a high efficiency parallel double-grating system to generate scalable rainbow illumination by simply adjusting the distance between the two. In the camera end, we exploit a varifocal encoded DOE lens to accommodate different sizes of the rainbow illumination, ranging from 15mm

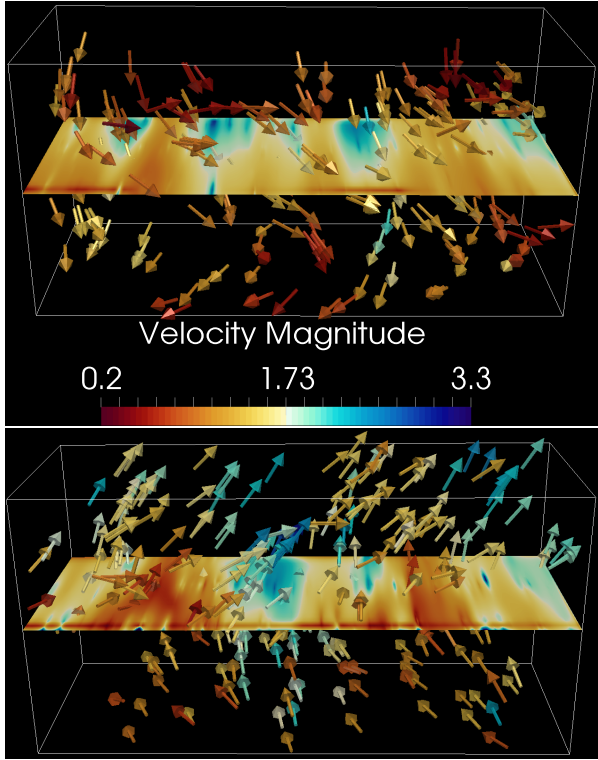


Figure 7: Flow vector visualizations for the fluid flow captured in rainbow sizes of 50mm (top) and 30mm (bottom).

to 50mm. Moreover, we propose a truncated consensus ADMM algorithm to reconstruct 3D particle distributions. Our algorithm is 5× faster than the prior arts. The reconstruction quality factor is also improved significantly for a series of density levels.

Similar to [13], the axial resolution is still a limitation for the proposed system. Specifically, two factors determine the axial resolution: the spectral resolution of the illumination, and the spectral resolution of the camera. The illumination spectrum spreads continuously over the volume width, thus the wider the volume is, the finer spectral resolution it reveals. However, representing full spectral information by only three color channels in an RGB camera leads to metamerism, which adds to the ambiguity to resolve spectral features by the camera. The benefit of the increased illuminating spectral resolution could not compensate for the loss of spectral information, hence the axial resolution is decided by the camera spectral resolution. Capturing more color channels can enhance the spectral resolution on the camera side, however, high resolution, multi-spectral video cameras are not readily available for high-res, video-rate capture as required by PIV.

Our system could be further improved in future work. First, although the light efficiency has been significantly improved compared to existing rainbow generation (e.g. linear

variable filter), the double-grating system still suffers from light loss in undesired diffraction orders. This could probably be addressed with the use of prisms instead of blaze gratings, although the prisms would have to be quite large, which adds to the bulk of the system, as well as its cost. Second, instead of using plasma white light source, a supercontinuum white light laser could be employed to improve the SNR, and hence smaller and less reflective particles could be tracked. Because of the reconfigurability of our system, it is fairly straightforward to apply this technique to both large scale and microscopic PIV applications.

References

- [1] S. Boyd, N. Parikh, E. Chu, B. Peleato, and J. Eckstein. Distributed optimization and statistical learning via the alternating direction method of multipliers. *Foundations and Trends in Machine Learning*, 3(1):1–122, 2011.
- [2] B. Choudhury, R. Swanson, F. Heide, G. Wetzstein, and W. Heidrich. Consensus Convolutional Sparse Coding. In *Proc. CVPR*, pages 4280–4288, 2017.
- [3] E. A. Deem, Y. Zhang, L. N. Cattafesta, T. W. Fahringer, and B. S. Thurow. On the resolution of plenoptic PIV. *Meas. Sci. & Techn.*, 27(8):084003, 2016.
- [4] G. E. Elsinga, F. Scarano, B. Wieneke, and B. W. van Oudheusden. Tomographic particle image velocimetry. *Exp. in Fluids*, 41(6):933–947, 2006.
- [5] T. W. Fahringer, K. P. Lynch, and B. S. Thurow. Volumetric particle image velocimetry with a single plenoptic camera. *Meas. Sci. & Techn.*, 26(11):115201, 2015.
- [6] F. Heide, Q. Fu, Y. Peng, and W. Heidrich. Encoded diffractive optics for full-spectrum computational imaging. *Sci. Rep.*, 6, 2016.
- [7] M. Levoy, R. Ng, A. Adams, M. Footer, and M. Horowitz. Light field microscopy. *ACM TOG*, 25(3):924–934, 2006.
- [8] K. Lynch, T. Fahringer, and B. Thurow. Three-dimensional particle image velocimetry using a plenoptic camera. AIAA, 2012.
- [9] R. Ng, M. Levoy, M. Brédif, G. Duval, M. Horowitz, and P. Hanrahan. Light field photography with a hand-held plenoptic camera. *CSTR*, 2(11):1–11, 2005.
- [10] Y. Peng, Q. Fu, F. Heide, and W. Heidrich. The Diffractive Achromat – Full Spectrum Computational Imaging with Diffractive Optics. *ACM TOG*, page 4, 2016.
- [11] F. Scarano. Tomographic PIV: principles and practice. *Meas. Sci. & Techn.*, 24(1):012001, 2012.
- [12] S. Shi, J. Wang, J. Ding, Z. Zhao, and T. New. Parametric study on light field volumetric particle image velocimetry. *Flow Meas. & Instr.*, 49:70–88, 2016.
- [13] J. Xiong, R. Idoughi, A. A. Aguirre-Pablo, A. B. Aljedaani, X. Dun, Q. Fu, S. T. Thoroddsen, and W. Heidrich. Rainbow particle imaging velocimetry for dense 3D fluid velocity imaging. *ACM TOG*, 36(4):36, 2017.
- [14] R. Zhang and J. Kwok. Asynchronous distributed ADMM for consensus optimization. In *Proc. ICML*, pages 1701–1709, 2014.